Curvature effects on the E_{33} and E_{44} exciton transitions in semiconducting single-walled carbon nanotubes

Erik H. Haroz,[1,†] Sergei M. Bachilo,[2] R. Bruce Weisman,[2] and Stephen K. Doorn[1,*]
[1]*Chemistry Division, Los Alamos National Laboratory, Los Alamos, New Mexico 87545, USA*
[2]*Department of Chemistry, Richard E. Smalley Institute for Nanoscale Science and Technology, and Center for Biological and Environmental Nanotechnology, Rice University, 6100 Main Street, Houston, Texas 77005, USA*
(Received 16 October 2007; revised manuscript received 11 December 2007; published 7 March 2008)

The E_{33} and E_{44} optical transitions of small diameter (0.7–1.2 nm) semiconducting single-walled carbon nanotubes are probed using deep blue (415–465 nm) resonance Raman spectroscopy and photoluminescence excitation spectroscopy in the UV and blue regions (280–488 nm). Individual radial breathing mode features, as well as Raman and photoluminescence excitation maxima, are assigned to specific nanotube chiralities. The chiral angle dependence of Raman intensity within a given $2n+m$ branch is found to continue, as does the trend toward increased excitation linewidths and weaker Raman intensities as higher lying transitions are accessed. The semiconducting E_{33} and E_{44} transition energies obtained for the largest observed diameters confirm recent results [P. T. Araujo *et al.*, Phys. Rev. Lett. **98**, 067401 (2007)] that show that these transitions reside on a blueshifted scaling-law line, separate from that describing E_{11} and E_{22} behaviors. Energies for nanotubes with diameter less than 0.9 nm, however, are not explained by any previous scaling-law fits. This behavior at small diameters is interpreted in terms of both a crossing over of the E_{33} and E_{44} energy trend lines for a given $2n+m$ branch and a chirality dependence in the many-body exciton effects that becomes significant at high curvatures.

DOI: 10.1103/PhysRevB.77.125405 PACS number(s): 78.67.Ch, 73.22.−f, 78.30.−j, 78.55.−m

I. INTRODUCTION

Advances in photoluminescence excitation (PLE) and resonance Raman spectroscopy of single-walled carbon nanotubes have led to definitive assignment of electronic and vibrational spectral features to their corresponding nanotube chiralities. The assignments are facilitated by the occurrence of patterns that group the PLE[1] or Raman radial breathing mode (RBM)[2–5] spectral features according to similar $2n+m$ "branches." Individual features may thus be paired unambiguously with their corresponding nanotube structural indices (n,m). These assignments have led to the development of useful semiempirical formulas for the calculation of E_{11} and E_{22} transition energies for semiconducting[1,5,6] and metallic[5,7] nanotube types. Experimentally based Kataura plots[8] of transition energy as a function of nanotube diameter or RBM frequency have also resulted.[3–6,9,10]

Such accurate assignments and development of the experimentally based Kataura plots are of great utility for characterizing nanotube sample composition and are important aids for the development of methods for selective synthesis, understanding of selective reaction chemistry and separations, as well as for understanding chirality-dependent effects on a variety of nanotube photophysical behaviors. The experimental energies and Kataura plots have guided theoretical efforts at describing energies and electronic structure based on an excitonic description.[11–18] Incorporation of the relevant many-body effects into an extended tight binding description of nanotube electronic structure now yields good agreement with observed E_{11} and E_{22} values.[16,19]

Extending optical studies into the higher lying E_{33} and E_{44} transitions is of interest for both theoretical and applied reasons. This is an important excitation region for sample characterization via Raman since commonly used visible excitation lines (e.g., 532, 514, and 488 nm) are capable of accessing this region, particularly for the larger diameter nanotubes generated by chemical vapor deposition,[20,21] laser-oven,[22,23] and vertical-array[24,25] growth methods commonly used for producing nanotubes for a wide range of electronics and materials applications. To better understand the electronic, optical, and materials properties of such nanotubes, it is necessary to correlate their behaviors to the structure. This requires accurate Kataura plots covering the E_{33} and E_{44} transition regions, similar to those now available for the lower lying E_{11} and E_{22} transitions. Analogously to the lower energy transitions, it will also be important to determine if accurate semiempirical or even first-principles analytical expressions can be developed for facile assignment of spectroscopic features in PLE and RBM spectra. From a more fundamental standpoint, expanded studies of the E_{33} and E_{44} region are necessary for developing a more complete understanding of the underlying electronic structure at higher energies. Such studies, for example, will allow the assessment of whether or not trends observed in excitonic behavior and exciton-phonon coupling continue at higher energies.

Recent resonance Raman work by Araujo *et al.*[10] has probed the E_{33} and E_{44} transitions for a large number of nanotube chiralities in the 1.1–2.3 nm diameter (d_t) range. The observed transition energies were described in terms of a nonlinear scaling law analysis that accounts for many-body exciton effects.[12,15,19] It was demonstrated that distinctly different behavior is observed for the E_{33} and E_{44} transitions, in comparison to those for E_{11} and E_{22}.[10] Similar results on a small set of index-identified single nanotubes in the diameter range of 1.4–2.4 nm have been reported more recently.[26] The $1/d_t$ dependence observed in the deviation between the higher and lower transitions points to a change in excitonic behavior at higher energies. The results of Araujo *et al.* have produced new physical insight into the behavior of the higher lying transitions in carbon nanotubes, with these results ulti-

mately demonstrating that the E_{33} and E_{44} transitions cannot be described by simple extensions of E_{11} and E_{22} patterns. Additionally, those results have shown that the nonlinear scaling laws can be used as an accurate basis for calculating Kataura plots useful for identifying spectral features at these higher energies.

It remains an open question, however, whether or not the large diameter E_{33} and E_{44} scaling-law behavior holds for smaller diameter nanotubes. In general, such highly curved nanotubes are known to display unique behaviors not observed for large diameters. For example, trigonal warping and curvature effects on observed transition energies become much more pronounced at smaller diameters.[27,28] RBM frequencies also begin to show deviations from expected trends near the small diameter limit.[2,19,29] It is therefore important to probe how E_{33} and E_{44} respond at small diameters as well. We present here resonance Raman excitation results for small diameter (0.7–1.2 nm) high pressure CO (HiPco)-produced nanotubes, in the region of 415–465 nm excitation. To complement the Raman data, we also present PLE data covering the region of 280 nm to 488 nm excitation. The blue and UV excitation results allow the assignment of 41 E_{33} and E_{44} spectral features to specific nanotube chiralities. Further analysis of the data confirms that trends in excitation linewidth and exciton-phonon coupling dependent intensities observed at lower energies continue into the higher lying transitions. However, we find that transition energies for nanotubes with diameter less than 0.9 nm are not well modeled by any previous scaling-law fits. We find that this behavior at small diameters can be explained in terms of both a crossing over of the E_{33} and E_{44} energy trend lines within a given $2n+m$ branch and a chirality dependence of many-body exciton effects that becomes significant at small diameters.

II. EXPERIMENT

Spectra were obtained from aqueous suspensions of as-produced HiPco nanotubes (Rice University batch HPR-120.5). We added 20 mg of raw nanotubes to 100 ml of 1% by weight sodium dodecyl sulfate in D_2O. These were dispersed by shear mixing (10 min), followed by ultrasonication (10 min at 500 W). The resulting suspension was ultracentrifuged at 120 000 g for 4 h. Spectroscopic samples were taken from the top 80% of the decant.

Resonance Raman spectroscopy was performed in a backscattering configuration with tunable dye laser excitation (using stilbene dye) scanned from 465 to 415 nm (2.67–2.99 eV) in 2 nm steps. Excitation power was maintained at 25 mW. Individual Stokes-shift spectra were obtained as 5 min integrations using a charge coupled device camera mounted on a SPEX triple monochromator. The frequency of each carbon nanotube spectrum was calibrated at each excitation wavelength with the nonresonance Raman spectrum of 4-acetamidophenol. Intensities were corrected for instrument response using a calibration curve obtained by fitting the intensity versus excitation wavelength curve of 4-acetamidophenol with a third order polynomial function. All Raman spectra were taken at room temperature and ambient pressure.

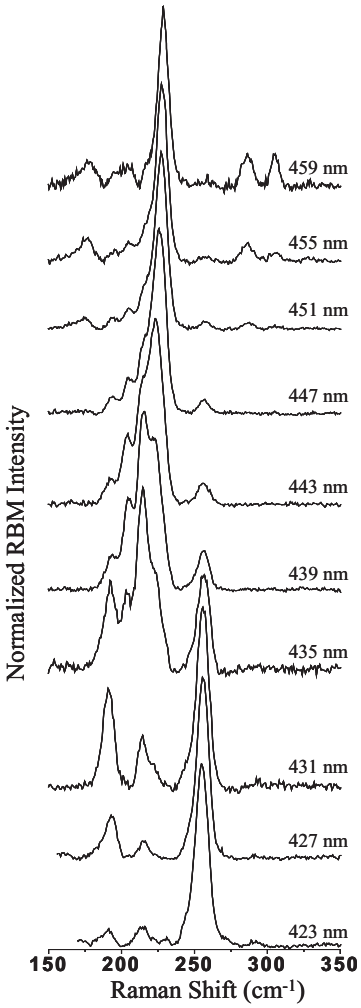

FIG. 1. Representative carbon nanotube RBM spectra for different excitation wavelengths. Individual spectral intensities are normalized with respect to the most intense peak in each spectrum for clarity.

We acquired quantum-corrected two-dimensional (2D) excitation-emission spectra of photoluminescence on a Fluorolog-3-211 (HORIBA Jobin-Yvon). Excitation light with a 5 nm bandwidth in the wavelength range from 280 to 488 nm (4.43–2.54 eV) was obtained from a Xe lamp using a double monochromator. Nanotube emission was measured from 800 to 1570 nm with a single-channel cooled InGaAs detector via a monochromator with 6 nm bandpass. Spectra were acquired with 2 nm steps in both excitation and emission wavelengths. Individual spectra were acquired with 1 s per point integration times and were repeated, as required, to ensure reproducibility and to improve signal to noise ratio.

III. RESULTS

A. Raman spectra

Raman spectra representative of those obtained across the excitation range are shown in Fig. 1 for the RBM region of

the spectrum. Spectra show the oscillatory behavior observed at lower excitation energies, for which features from different $2n+m$=const branches grow in and decay sequentially as excitation energy is varied. Two main $2n+m$ branches are observed in our data, centered at around 225 and 250 cm^{-1}. Additional features not associated with these two main groupings are also observed, particularly at lower excitation energies. Assignment of these features to specific chiralities requires correlation of RBM frequencies to excitation energies and matching of the resultant branching patterns to theoretical expectations.

Spectral patterns arising from correlations of transition energy to nanotube diameter or RBM frequency have been instrumental in the assignment of spectral features to specific (n,m) designations.[5,10] For example, RBM features belonging to nanotubes of the same $2n+m$=const branches show "hooked" energy spread branching patterns resulting from deviations of observed transition energies from an idealized tight binding description of armchair energies. As one progresses from the near-armchair chiralities to near-zigzag chiralities within a given $2n+m$ branch, these deviations increase, resulting in the familiar pattern. Such patterns are readily observed when RBM frequencies are plotted against excitation energy in a 2D intensity map and permit ready grouping of individual features by branch. Such a plot is shown in Fig. 2(a) for our Raman data. Figure 2(a) allows one to conclude, for example, that the RBM features between 204 and 230 cm^{-1}, in the excitation region of 2.7–2.85 eV, belong to a single $2n+m$ branch. Another branch is clearly delineated in the frequency range of 230–256 cm^{-1}, for excitation energies ranging from about 2.85 to 3 eV.

Our strategy for the assignment of the observed RBM features to specific (n,m) designations is to first compare the experimental Kataura plot results of Fig. 2(a) to features expected from an extended tight binding (ETB) model[30] that incorporates many-body effects resulting from exciton formation.[16,19] Excellent agreement has been demonstrated between the ETB model and E_{11} and E_{22} transition energies.[19] Patterns will be correlated between the two plots to assign chiralities. In the event that multiple plausible choices or overlapping of similar patterns exists for specific RBM features, assignments will be made via reference to other features occurring in the spectra to produce a globally consistent comparison. Such an approach works best when complete $2n+m$ branches are present for comparison. Thus, the two main branches that we observe will be assigned first and will then be used to anchor the spectral behavior for the identification of the remaining features that are not clearly linked to other branches (for example, the lone RBM feature occurring at 193 cm^{-1} and centered at an excitation energy near 2.86 eV).

As a reference point for our assignments, a detail of the ETB results for the region centered around our Raman excitation energies is shown in Fig. 2(b). Features found in this plot belong primarily to E_{11}^{M}, E_{33}^{S} [both mod$(n-m,3)=1$ and 2 types, referred to hereafter as "mod 1" and "mod 2," respectively] and E_{44}^{S} (mod 2 type) transitions, where M and S refer to metallic and semiconducting species, respectively. Two branches (corresponding to E_{33}^{S} transitions for $2n+m$ =23 and 26) that appear in the ETB plot (highlighted by

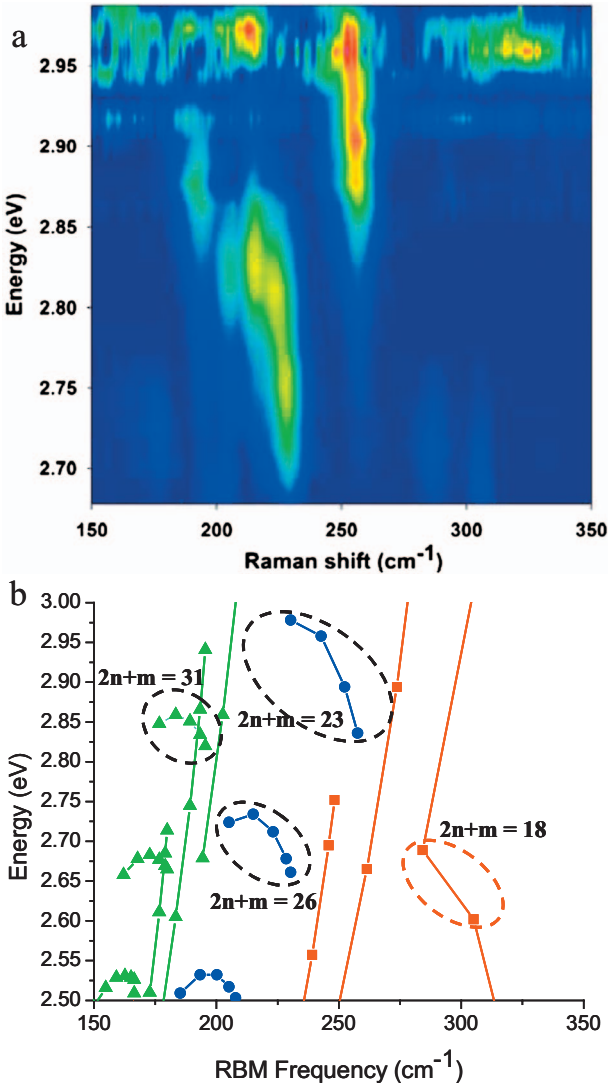

FIG. 2. (Color) (a) 2D intensity map showing RBM intensity behavior as the excitation wavelength is changed. The map shows grouping of the main RBM features into $2n+m$=const branches. (b) ETB predicted (Ref. 16) features within the same energy and RBM frequency region for mod 2 semiconductors (E_{33} and E_{44}, green triangles), mod 1 semiconductors (E_{33}, blue circles), and metallics (E_{11}, red squares). The highlighted branches correspond to the observed features in part (a) and in Fig. 1.

dashed ellipses) are good candidates for the features observed in the experimental data. Although the transition energies do not match, they are the only features in the ETB plot with RBM frequencies that are well matched to the experimental frequencies. Additionally, the two branches in the experimental data are separated in energy by the same relative amounts as the branches appearing in the ETB plot. Thus, we assign the two branches centered at RBM frequencies of 225 and 250 cm^{-1} to $2n+m$=23 and 26, respectively. The higher frequency RBMs in each branch correspond to the near-zigzag chiralities, allowing the final assignment of individual RBMs to specific chiralities, as shown in Table I. The blueshift in E_{33}^{S} transition energies from ETB expectations is consistent with the behavior previously observed[10] and is discussed below.

TABLE I. Observed values for RBM frequency (ω_{RBM}), third optical transition energy (E_{33}), and transition linewidths (Γ_{33}) obtained from the Raman data for a given (n,m) chirality nanotube with diameter d_t and chiral angle θ.

(n,m)	d_t (nm)	θ (deg)	ω_{RBM} (cm^{-1})	E_{33} (eV)	Γ_{33} (meV)
(13,0)	1.231	0	230	2.72	115
(12,2)	1.027	7.59	228	2.73	123
(11,4)	1.054	14.92	224	2.78	130
(10,6)	1.097	21.79	216	2.81	118
(9,8)	1.154	28.05	204	2.81	115
(11,1)	0.903	4.31	256	2.88	113
(10,3)	0.924	12.73	251		
(9,5)	0.965	20.63	242		
(8,7)	1.018	27.8	230		
(14,3)	1.231	9.52	193	2.86[a]	111

[a]Energy is for E_{44} (see discussion).

The RBMs found at 286 and 305 cm^{-1} with lower energy excitation (451–463 nm, see Fig. 1) are assigned to the E_{11}^M features circled in red in Fig. 2(b). The observed frequencies are an excellent match and, although we are unable to complete the excitation profiles on the low energy side for these species, the energy range over which we observe them is in good agreement with the ETB-based Kataura plot (as expected for E_{11}^M, see Ref. 10). These features are therefore assigned as the (6,6) and (7,4) nanotubes of the $2n+m=18$ branch. This assignment is also consistent with previous resonance Raman studies.[5]

Assignment of the 193 cm^{-1} RBM centered at ~2.86 eV excitation energy is more problematic. As seen in Fig. 2(b), there are several candidates corresponding to E_{33} or E_{44} excitations of a number of mod 2 semiconducting chiralities (green triangles) from the $2n+m=28$ or 31 branches. The closest in frequency are the (15,1), (14,3), and (10,8) chiralities at 195.5, 193.3, and 194.5 cm^{-1}, respectively. We assign this feature as the (14,3) RBM due to its close match to both the expected frequency and the relative position of its transition energy with respect to that for the $2n+m=23$ and 26 branches (see also later discussion).

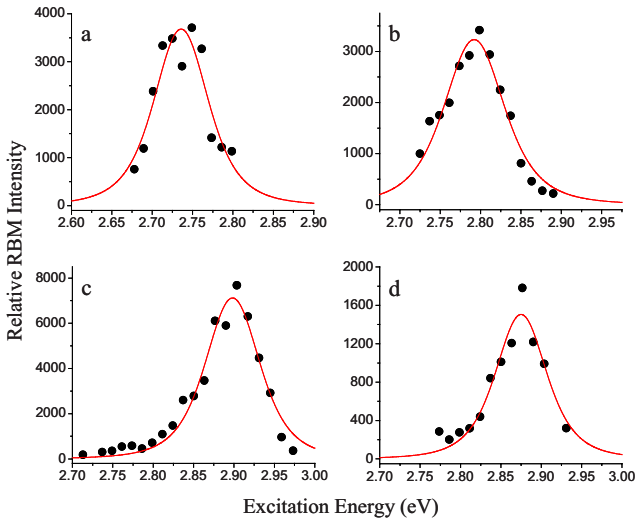

FIG. 3. (Color online) Resonance Raman excitation profiles for four selected nanotube chiralities. Lines are fits according to Eq. (1) of the experimental data (dots), from which Γ values are extracted: (a) (13,0), Γ=115meV; (b) (11,4), Γ=130 meV; (c) (11,1), Γ=113 meV; (d) (14,3), Γ=111 meV.

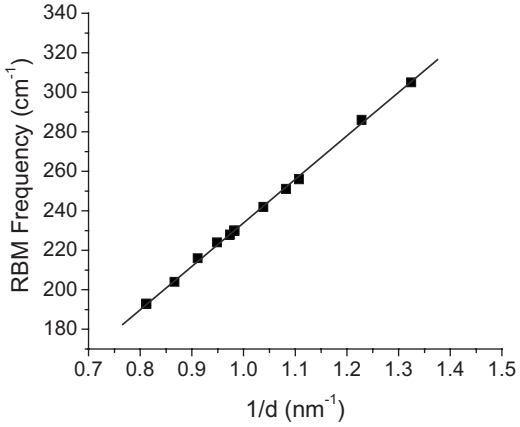

FIG. 4. Plot of RBM frequency as a function of inverse nanotube diameter $(1/d)$. The line is a linear fit to the experimental data points (squares), yielding the parameters $A=219.3$ nm cm^{-1} and $B=14.7$ cm^{-1} from Eq. (2).

Knowledge of which $2n+m$ branches are responsible for the observed features in Fig. 2(a) gives direct information on the number of chiralities, and their expected frequencies, that should appear in the RBM spectrum for that branch. This was used as an aid to guide the deconvolution of single RBM spectra into their individual chirality components. Extraction of the individual components allowed the construction of the excitation profiles for each observed chirality. Example profiles for four species are shown in Fig. 3. The experimental excitation profiles were then fit to the resonance Raman line shape function for Stokes scattering,[5,31,32]

$$I_{RBM} = \frac{M}{\left[(E_{ii} - E_{laser})^2 + \frac{\Gamma^2}{4}\right]\left[(E_{ii} - E_{laser} - \hbar\omega_{RBM})^2 + \frac{\Gamma^2}{4}\right]}. \quad (1)$$

Here, M incorporates absorption and exciton-phonon coupling matrix elements and sampling conditions, while E_{ii} and E_{laser} are transition and excitation energies, respectively. Fits to Eq. (1) were performed with the RBM frequency (ω_{RBM}) fixed to the experimental values and were used to extract the values for the transition energy E_{33} and broadening factor Γ_{33} as adjustable fitting parameters. The results are summarized in Table I.

Finally, we plot in Fig. 4 the observed RBM frequencies as a function of inverse diameter (d_t) to obtain the coefficients A and B in the usual expression used to relate the two parameters,

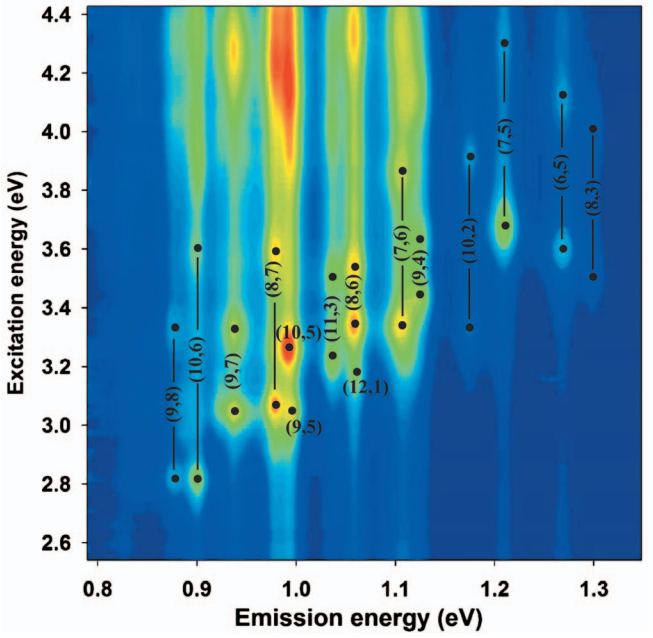

FIG. 5. (Color) 2D intensity map showing the nanotube photoluminescence intensity as a function of emission energy, as the excitation energy is varied. Chirality assignments for selected E_{33} and E_{44} features are highlighted.

$$\omega_{\mathrm{RBM}} = A/d_t + B. \tag{2}$$

A best fit line to the experimental data yields $A = 219.3$ nm cm^{-1} and $B = 14.7$ cm^{-1}, in accord with other values reported in the literature.[5,10] The excellent linear fit provides additional confidence that our chosen (n,m) assignments are correct.

B. Photoluminescence excitation spectra

A 2D PLE intensity map for our sample is shown in Fig. 5. The branching patterns observed in the analogous Raman excitation plot are not as well defined for the PLE map due to the density of spectral features occurring over most of this energy region. However, we were still able to make definitive assignments for 31 E_{33} and E_{44} spectral features.

PL features were assigned by first identifying their E_{11} emission energy. For each emission energy corresponding to a PL feature, an exhaustive list of possible (n,m) assignments was generated from empirical predictions based on fitted PLE data.[6] Certain chiralities [such as the (6,5), (8,6), (8,7), (9,7), and others] have E_{11} emission energies that are well isolated from other chiralities such that only one (n,m) is possible, allowing both the E_{33} and E_{44} excitation energies to be unambiguously assigned for them. In cases where the emission energy was not sufficiently isolated as to result in only one (n,m), the list of possible (n,m) assignments was compared to the known (n,m) chiralities present in this particular sample, as determined by PLE spectroscopy via E_{22} excitation. This list of known chiralities was used to constrain the possible assignments for the higher order PL features. For instances where a single (n,m) assignment was still indeterminable and where the potential assignments displayed a difference in mod characteristic (i.e., one assignment is mod 1, whereas the other is mod 2), an examination of the energy difference between the E_{33} and E_{44} features, ΔE, was made. Nanotubes displaying E_{33}/E_{44} features that are relatively closely spaced in energy ($\Delta E < 300$ meV) were considered to be more likely of the mod 2 variety, while nanotubes with fairly large ΔE were considered more likely to be mod 1. We also looked at any closely spaced E_{33}/E_{44} features for possible phonon-assisted photoluminescence due to either RBM or G-mode phonons. Such phonon-assisted PL features were not included in our reported data.

Additionally, we were able to use the Raman assignments obtained in the previous section to "anchor" certain parts of the PLE map, further enabling assignments of additional chiralities [such as the (10,6) and (9,8) and nearby chiralities]. Finally, so as to confirm these assignments as well as suggest assignments for undetermined features, patterns observed in an analogous plot of correlated ETB energies, while offset from the experimental data in a manner similar to that found in the Raman data, provided a useful guide for the assignment of the final transitions not obtained by the above approaches. The resulting assignments and E_{33} and E_{44} transition energies are highlighted in Fig. 5 and listed in Table II. The listed features (and energies used in the analysis discussed below) are only for those chiralities that we feel have been assigned with the highest confidence.

TABLE II. Observed values for third (E_{33}) and fourth (E_{44}) optical transition energies obtained from the PLE data for a given (n,m) chirality nanotube with diameter d_t and chiral angle θ.

(n,m)	d_t (nm)	θ (deg)	E_{33} (eV)	E_{44} (eV)
(6,4)[a]	0.692	23.41	3.93[a]	
(6,5)	0.757	27	3.6	4.11
(8,3)[a]	0.782	15.3	3.53[a]	4.02[a]
(7,5)	0.829	24.5	3.68	4.29
(7,6)	0.895	27.46	3.34	3.87
(10,2)[a]	0.884	8.95	3.33[a]	3.91[a]
(9,4)[a]	0.916	17.48	3.43[a]	3.62[a]
(8,6)	0.966	25.28	3.35	3.54
(11,1)	0.916	4.31		4.24
(9,5)	0.976	20.63	3.05	
(8,7)	1.032	27.8	3.07	3.59
(12,1)[a]	0.995	3.96	3.18[a]	
(11,3)[a]	1.014	11.74	3.23[a]	3.51[a]
(10,5)	1.05	19.11	3.27	
(9,7)	1.103	25.87	3.05	3.33
(10,6)	1.111	21.79	2.82	3.6
(9,8)	1.17	28.05	2.82	3.33
(10,8)	1.24	26.33	2.79	3.1

[a]Energies for E_{33} and E_{44} for these chiralities must be exchanged. Because of the crossover effect (see discussion), energy ordering is reversed in these cases.

IV. DISCUSSION

A. Transition level and Raman intensities

It is important to note that the intensities observed in the RBM spectra obtained here are about an order of magnitude weaker than found for spectra obtained at resonance with the E_{22} transitions. This behavior is also reported in Ref. 10, in which RBM features resonant with E_{33} or E_{44} transitions are significantly weaker than those resonant with E_{11} or E_{22}. These reduced intensities for the higher lying nanotube transitions continue the trend previously observed in Ref. 33. In that work, RBM intensities observed at resonance with E_{22} excitation were significantly lower (by 1 or more orders of magnitude) than those observed at resonance with E_{11} excitation for identical nanotube chiralities. Loss of intensity was observed for all chiralities, despite the expectation that it should increase for mod 2 nanotubes due to an increase in the magnitude of their exciton-phonon coupling (see below). The decreased intensities were attributed to the more rapid dephasing of the E_{22} exciton, as manifested by an increase in gamma values.[33] Resonance linewidths were found to increase from 20–30 meV for E_{11} to 50–70 meV for E_{22}. We find here (Table I) that gamma values continue to increase on going to E_{33} excitation, with observed values being twice those found for E_{22}, and ranging from 110 to 130 meV. These results suggest that exciton decay rates will further increase as one excites to higher energy, as is consistent with the stronger vibronic interactions and accelerated relaxation processes found at higher excitation energies in molecular photophysics.

An additional contributing factor to the intensity behavior within the E_{33} and E_{44} transitions is how the exciton-phonon coupling is affected at these excitation levels. For example, it has been observed that the chiral angle dependence of exciton-phonon coupling results in a decrease in RBM intensity as the chiral angle (θ) increases within a particular $2n+m$ branch.[4,34,35] Such a trend is, in fact, observed for the $2n+m=26$ branch with E_{33} excitation. Progressing from the zigzag (13,0) ($\theta=0°$) to near-armchair (9,8) ($\theta=28°$) chiralities, we observe a steady decrease in intensity of the respective RBM. Another anticipated effect on the exciton-phonon coupling is its dependence on the semiconductor type. Previous reports[2,34,36] have shown that with E_{22} excitation, mod 2 tubes have larger coupling (and therefore RBM intensity) than mod 1. In general, this dependence is reversed in E_{11} excitation and is also expected to reverse for the E_{33} transition. Thus, for excitation into E_{33}, we should expect to see primarily mod 1 RBM features. This is in agreement with the chiralities observed in our Raman spectra. Except for the (14,3) chirality, all observed semiconductors are mod 1. That the mod 2 (14,3) chirality is observed suggests that resonance excitation is with E_{44} rather than E_{33} for this nanotube. We confirm this hypothesis in the next section.

B. Transition crossing and observed energies

E_{33} transition energies determined from the Raman and PLE results are on average 70 meV larger than those calculated in the ETB approach. This positive deviation is in good alignment with the previous results of Araujo *et al.*[10] The trends found in the E_{44} energies are more complex. The positive deviations in observed energies can be understood in terms of how the exciton many-body contributions change as one accesses the higher order nanotube transitions. The behavior of these many-body effects can be extracted from the experimental transition energies by using an analysis similar to that used in Ref. 10. We find that applying this analysis to our data reveals interesting behavior that is not evident in the previous analysis, as applied to larger diameter nanotubes.

The nanotube transition energy can be dissected into contributions from the diameter-dependent single-particle energy expected from quantum confinement of the 2D electronic structure of graphene, the chiral angle (θ) dependent effects of trigonal warping, and many-body excitonic effects. The quantum confinement energy may be given as $h\nu_F(4p/3d_t)$, where ν_F is the Fermi velocity, d_t is the nanotube diameter, and $p=1,2,3,4,5$ for E_{11}^S, E_{22}^S, E_{11}^M, E_{33}^S, and E_{44}^S, respectively.[37] Trigonal warping perturbation[27,28] raises or lowers these energies in a chiral angle dependent fashion to produce the now-familiar branching patterns observed in PLE and Raman data.[1,3–5,10] This contribution may be approximated by the term $\beta_p \cos 3\theta/d_t^2$, where β_p is +0.42 for E_{33} (−0.40 for E_{44}) for mod 2 nanotubes and is −0.42 for E_{33} (+0.40 for E_{44}) for mod 1 nanotubes.[10] What remains after removal of this term and the linearly dependent quantum confinement term from the experimentally determined transition energies is the excitonic contribution of the many-body effects, which may be approximated by a logarithmic scaling of energies,[12,19] also dependent on p/d_t. Each of these contributions is expressed in[10]

$$E_{ii}(p,d_t) - \beta_p \cos 3\theta/d_t^2 = a\frac{p}{d_t}\left(1 + b\log\frac{c}{p/d_t}\right), \qquad (3)$$

in which a, b, and c are fitting parameters and $E_{ii}(p,d_t)$ is the experimentally determined transition energy.

In Fig. 6(a), we subtract the trigonal warping term from our experimentally determined E_{33}^S and E_{44}^S transition energies and plot the result as a function of p/d_t. These results are compared to two different trend lines. The first (lower line) is the result of Eq. (3) when applied to E_{11}^S and E_{22}^S transition energies, with a, b, and c equaling 1.049 eV nm, 0.456, and 0.812 nm^{-1}, respectively.[10] The work of Araujo *et al.* showed that the E_{33}^S and E_{44}^S energies deviate from this behavior by the term $0.305/d_t$. We show the resulting E_{33}^S and E_{44}^S trend line as the second, upper curve. Inspection of Fig. 6(a) leads to two notable observations. The first is that while the majority of the observed chiralities appear to fall on a smooth trend line, a handful of designated chiralities (highlighted by circles) add significant scatter to this pattern. The second observation is that although energies for the largest diameter nanotubes in our data set (0.9–1.2 nm) reproduce with excellent agreement the E_{33}^S and E_{44}^S trend line of Ref. 10, energies for the smallest diameter nanotubes show a significant negative deviation from this trend (beginning at d_t values of about 0.9 nm). This deviation is most dramatically shown by the E_{44} value for the (6,5) chirality, which is so low that it reaches the original E_{11} and E_{22} scaling-law trend

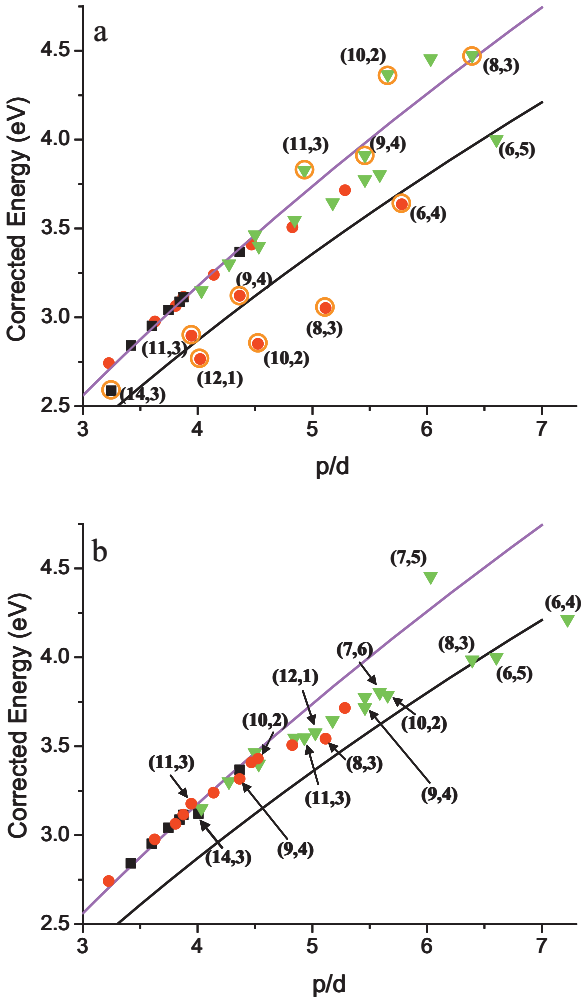

FIG. 6. (Color) (a) Corrected E_{33} and E_{44} transition energies ($E_{\mathrm{exp}}-\beta_p \cos 3\theta/d_t^2$) as a function of p/d, where $p=4$ and 5, respectively. E_{33} data are obtained from Raman (black squares) and PLE (red circles) measurements, while E_{44} data (green triangles) are obtained from the PLE measurement. Energy assignments to E_{33} and E_{44} features are chosen directly from their respective ordering from the experimental results. Results are compared to scaling-law lines from Ref. 10 for E_{33} and E_{44} (upper line) and E_{11} and E_{22} (lower line behavior), see Eq. (3). Chiralities showing significant scatter from the scaling-law behavior are designated and highlighted by circles. (b) The data of part (a) replotted after correcting the energy ordering of the (14,3), (12,1), (11,3), (10,2), (9,4), (8,3), and (6,4) chiralities for the effect of branch crossover.

line. We address first the problem of the appearance of significant scatter for certain chiralities. The negative deviation of the E_{33} and E_{44} scaling behavior for small diameter nanotubes is discussed in the following section.

The large deviation and scatter from the E_{33} and E_{44} scaling-law line for the (6,4), (8,3), (9,4), (10,2), (11,3), and (12,1) chiralities is a previously unobserved manifestation of a trigonal warping effect that only becomes evident as one accesses the higher lying transitions of small diameter nanotubes. This behavior is, in a sense, a more extreme consequence of the underlying causes of the branching energy spread found along a given $2n+m$ value. Within the graphite Brillouin zone, trigonal warping results in equienergy contours that are distorted from circles into a more triangular shape, with apex along the K-M line and base along the Γ-K line. For mod 2 semiconducting types, the E_{11} and E_{33} transitions originate in the K-M valley, while E_{22} and E_{44} originate from the Γ-K valley. As a result, as one goes from near-armchair to near-zigzag chiralities within a $2n+m$ branch, the E_{11} and E_{22} energies curve toward each other, as do the E_{33} and E_{44} energies. These higher order transitions occur in a region of greater trigonal distortion of the energy surfaces so that the difference between E_{33} and E_{44} energies can become quite small. In particular cases, the effect can even reverse the ordering of their energies. This reversal of energy ordering can be seen in a Kataura plot of ETB calculated energies vs RBM frequency (Fig. 7). In this plot, we see that for certain chiralities at these higher energies, the E_{33} and E_{44} energies are predicted to cross over. We note that the smallest diameter branches are most strongly affected by this phenomenon. Of the chiralities that we observe, the (6,4), (8,3), (9,4), (10,2), (11,3), and (12,1) nanotubes (highlighted in Fig. 7) would be expected to show this crossover effect. We conclude that the E_{33}/E_{44} crossover phenomenon is responsible for the scattered behavior of these chiralities seen in Fig. 6(a).

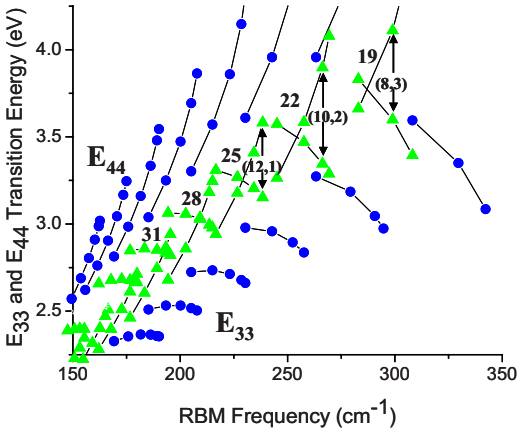

FIG. 7. (Color online) ETB calculated (Ref. 16) E_{33} and E_{44} transition energies as a function of RBM frequency for mod 1 (circles) and mod 2 (triangles) species. Branch crossover effect of E_{33} and E_{44} energy behaviors is illustrated, with specific chiralities and branches relevant to Fig. 6(a) highlighted.

The results shown in Fig. 7 suggest that, for these higher order transitions, the correct E_{ii} assignment is not necessarily obtained by simple ordering of spectral features according to transition energy. Specifically, for the (6,4), (8,3), (9,4), (10,2), (11,3), and (12,1) nanotubes, an exchange of the E_{33} and E_{44} energy assignments shown in Table II is indicated. To appropriately account for this assignment change in the analysis of Fig. 6(a), the correct values of β_p and p (determined by choice of E_{ii}) must be paired with the corresponding energies. Our results after applying this energy reordering are plotted in Fig. 6(b). A smooth behavior across the whole range of data is now seen. This analysis can therefore be taken as a strong experimental evidence supporting the energy crossover effect. Thus, at higher energies, care must be taken in assigning E_{ii} values to observed spectral features.

E_{ii} should not be deduced simply on the basis of energy ordering but more correctly from its basis in symmetry with respect to the K point, as defined by the ordering of the respective cutting lines.

One consequence of the minimization of the energy difference between E_{33} and E_{44} and the crossing over of these transitions in mod 2 nanotubes is the possibility of observing Raman interference effects.[38,39] While Raman interference could potentially impact the observed excitation profile for the (14,3) chirality, the symmetric appearance of the data [Fig. 3(d)] suggests that any interference effects are minimized. This is likely a result of the E_{33} transition strength being significantly reduced via exciton-phonon coupling effects.[33–36] For the remaining chiralities observed in the Raman spectra, interference effects are not likely since these are mod 1 nanotubes whose E_{33} and E_{44} energies spread away from each other (see Fig. 7).

Deviations from the trends found within the scaling-law analysis can thus be used to identify the energy crossover effect and may be used as an additional tool to aid in assigning spectral features. We apply this result to make a secure assignment of the (14,3) feature observed in the RBM Raman excitation profiles. As seen in Fig. 6(a), if this feature is identified as the E_{33} transition, a significant deviation from the scaling-law line results, in a region where excellent agreement is found for similar diameter nanotubes. Figures 2(b) and 6(b) show that crossover of the E_{33} and E_{44} transitions is expected to occur for this chirality. If the (14,3) spectral feature is instead assigned to the E_{44} transition, we find close agreement to the scaling-law trend [see Fig. 6(b)]. Assignment as the E_{44} feature also preserves the trend in expected intensities for mod 2 semiconductor types, as discussed in the previous section. Finally, we note that the (7,5) feature assigned as E_{44} also deviates significantly from the expected trends [Fig. 6(b)]. It is likely that this feature is instead an E_{55} transition. This revised assignment will also bring the (7,5) point into alignment with the generally observed trends.

C. Curvature effects on higher order exciton energies

The two different trend lines in Fig. 6 effectively illustrate the difference in behavior of SWNT excitonic energy contributions in higher energy transitions. The many-body effects contribute as the difference $(\Sigma - E_{bd})$ between the electron self-energy (Σ) and the exciton binding energy (E_{bd}). This difference is found to be significantly larger for E_{33} and E_{44} because the self-energy increases considerably relative to E_{bd} for higher order transitions[40] and is suggested to be the origin of the differing trend lines in Fig. 6. Additionally, at smaller diameters, Sato *et al.*[40] found a significant chiral angle dependence and/or energy spread in the E_{33} and E_{44} many-body contributions that is not present for E_{11} and E_{22}. The energy spread in the many-body term appears to arise primarily from E_{bd}. Thus, while the chiral angle dependence in E_{11} and E_{22} appears mainly as the branching energy spread in the single-particle energies, the energy spread in the many-body term adds a significant source of chiral angle dependence in E_{33} and E_{44}.

It is important to note, however, that the single-particle and many-body sources of energy spread contribute in opposite directions.[40] In the case of mod 2 semiconductors, for example, the single-particle contribution is positive, while that from the many-body chiral angle dependence is negative. Thus, when we apply the $\beta_p \cos 3\theta / d_t^2$ term to remove the single-particle energy spread, the negative-going component from the many-body effects remains. The net effect is that applying the $\beta_p \cos 3\theta / d_t^2$ term overcorrects for the energy spread behavior in small diameter nanotubes and results in the negative-going trend away from the E_{33} and E_{44} scaling-law lines shown in Fig. 6. This is predicted to be most pronounced for near-zigzag chiralities[40] and is supported by our data. In contrast, one would expect the opposite behavior for mod 1 semiconductors, with an overcorrection resulting in positive deviations from the scaling-law line for these nanotube types. However, the mod 1 nanotubes we observe in our results are near-armchair chiralities, for which the energy spread effect should be minimal. The negative-going trend in these types arises from another effect.

In general, the electron self-energy is expected to be only weakly dependent on the chiral angle.[40] For higher order transitions and smaller diameters, however, this expectation breaks down and a significant θ dependence is predicted.[40] In particular, in E_{44}, Σ for mod 1 nanotubes is expected to decrease significantly as the chiral angle increases. Near-armchair mod 1 chiralities should therefore show a significant negative-going trend in the plots of Figs. 6(a) and 6(b). This is, in fact, what we observe, with the effect most clearly being seen for the (6,5) and (7,6) chiralities. The decrease in Σ as θ increases is predicted to become less important in E_{33} and for mod 2 nanotubes, but it can be an additional minor source of the negative-going trend observed in our data.

V. CONCLUSIONS

Extending Raman and photoluminescence excitation profiling of nanotubes into the UV has provided access to higher lying exciton transitions for small diameter nanotubes and has allowed us to assign their E_{33} and E_{44} spectral features. This extended excitation range has demonstrated a further continuation of some previously observed trends, including exciton-phonon coupling trends, the increase in magnitude of Γ, and scaling-law behavior of the largest diameter nanotubes in our study. More importantly, however, this has also allowed the observation of unique curvature effects. We have experimentally verified an extension of trigonal warping effects by showing that the energy crossover behavior along selected $2n+m$ branch lines has physically observable consequences. Additionally, a number of predictions of recent theoretical studies[40] on the chirality dependence of many-body effects have now been experimentally verified. Our observation of a negative deviation from the large diameter E_{33} and E_{44} scaling-law trend line of Araujo *et al.*[10] clearly demonstrates the existence of these effects and also confirms the sign of chirality-dependent trends expected for both self-energy and binding energy. These results provide an experimental foundation for further probing the potential sensitiv-

ity of these spectral effects to nanotube environment. Recognizing and understanding the trends observed here can greatly assist in the assignment of spectral features in this increasingly crowded spectral region as the E_{ii} transitions tend to broaden and merge together. The scaling-law analysis can be a particularly powerful tool in that regard. This region will be a fruitful arena in which to further explore nanotube properties that become evident only at small diameters and high energies.

ACKNOWLEDGMENTS

We thank Ado Jorio for valuable discussions and for providing the ETB data used in Figs. 2 and 7. S.K.D. acknowledges support of the LANL LDRD program. R.B.W. and S.M.B. thank the NSF Center for Biological and Environmental Nanotechnology (EEC-0647452), the Welch Foundation (C-0807), and Applied NanoFluorescence, LLC for research support.

†Present address: Department of Electrical & Computer Engineering, Rice University, 6100 Main Street, Houston, TX 77005.
*Author to whom correspondence should be addressed; skdoorn@lanl.gov

[1] S. M. Bachilo, M. S. Strano, C. Kittrell, R. H. Hauge, R. E. Smalley, and R. B. Weisman, Science **298**, 2361 (2002).
[2] S. K. Doorn, D. A. Heller, P. W. Barone, M. L. Usrey, and M. S. Strano, Appl. Phys. A: Mater. Sci. Process. **78**, 1147 (2004).
[3] C. Fantini, A. Jorio, M. Souza, M. S. Strano, M. S. Dresselhaus, and M. A. Pimenta, Phys. Rev. Lett. **93**, 147406 (2004).
[4] H. Telg, J. Maultzsch, S. Reich, F. Hennrich, and C. Thomsen, Phys. Rev. Lett. **93**, 177401 (2004).
[5] J. Maultzsch, H. Telg, S. Reich, and C. Thomsen, Phys. Rev. B **72**, 205438 (2005).
[6] R. B. Weisman and S. M. Bachilo, Nano Lett. **3**, 1235 (2003).
[7] M. S. Strano, S. K. Doorn, E. Haroz, C. Kittrell, R. H. Hauge, and R. E. Smalley, Nano Lett. **3**, 1091 (2003).
[8] H. Kataura, Y. Kumazawa, Y. Maniwa, I. Umezu, S. Suzuki, Y. Ohtsuka, and Y. Achiba, Synth. Met. **103**, 2555 (1999).
[9] M. S. Strano, J. Am. Chem. Soc. **125**, 16148 (2003).
[10] P. T. Araujo, S. K. Doorn, S. Kilina, S. Tretiak, E. Einarsson, S. Maruyama, H. Chacham, M. A. Pimenta, and A. Jorio, Phys. Rev. Lett. **98**, 067401 (2007).
[11] T. Ando, J. Phys. Soc. Jpn. **66**, 1066 (1997).
[12] C. L. Kane and E. J. Mele, Phys. Rev. Lett. **93**, 197402 (2004).
[13] H. Zhao and S. Mazumdar, Phys. Rev. Lett. **93**, 157402 (2004).
[14] C. D. Spataru, S. Ismail-Beigi, L. X. Benedict, and S. G. Louie, Phys. Rev. Lett. **92**, 077402 (2004).
[15] V. Perebeinos, J. Tersoff, and P. Avouris, Phys. Rev. Lett. **92**, 257402 (2004).
[16] Ge. G Samsonidze, R. Saito, N. Kobayashi, A. Gruneis, J. Jiang, A. Jorio, S. G. Chou, G. Dresselhaus, and M. S. Dresselhaus, Appl. Phys. Lett. **85**, 5703 (2004).
[17] R. B. Capaz, C. D. Spataru, S. Ismail-Beigi, and S. G. Louie, Phys. Rev. B **74**, 121401(R) (2006).
[18] J. Jiang, R. Saito, Ge. G. Samsonidze, A. Jorio, S. G. Chou, G. Dresselhaus, and M. S. Dresselhaus, Phys. Rev. B **75**, 035407 (2007).
[19] A. Jorio, C. Fantini, M. A. Pimenta, R. B. Capaz, Ge. G. Samsonidze, G. Dresselhaus, M. S. Dresselhaus, J. Jiang, N. Kobayashi, A. Gruneis, and R. Saito, Phys. Rev. B **71**, 075401 (2005).
[20] A. Jorio, R. Saito, J. H. Hafner, C. M. Lieber, M. Hunter, T. McClure, G. Dresselhaus, and M. S. Dresselhaus, Phys. Rev. Lett. **86**, 1118 (2001).
[21] S. K. Doorn, L. Zheng, M. J. O'Connell, Y. Zhu, S. Huang, and J. Liu, J. Phys. Chem. B **109**, 3751 (2005).
[22] S. Arepalli, J. Nanosci. Nanotechnol. **4**, 317 (2004).
[23] S. Lebedkin, F. Hennrich, T. Skipa, and M. M. Kappes, J. Phys. Chem. B **107**, 1949 (2003).
[24] Y. Murakami, E. Einarsson, T. Edamura, and S. Maruyama, Carbon **43**, 2664 (2005).
[25] K. Hata, D. N. Futaba, K. Mizuno, T. Namai, M. Yumura, and S. Iijima, Science **306**, 1362 (2004).
[26] T. Michel, M. Paillet, J. C. Meyer, V. N. Popov, L. Henrard, and J. L. Sauvajol, Phys. Rev. B **75**, 155432 (2007).
[27] R. Saito, G. Dresselhaus, and M. S. Dresselhaus, Phys. Rev. B **61**, 2981 (2000).
[28] S. Reich and C. Thomsen, Phys. Rev. B **62**, 4273 (2000).
[29] J. Kurti, V. Zolyomi, M. Kertesz, and G. Y. Sun, New J. Phys. **5**, 125 (2003).
[30] V. N. Popov, New J. Phys. **6**, 17 (2004).
[31] M. A. Pimenta, A. Marucci, S. A. Empedocles, M. G. Bawendi, E. B. Hanlon, A. M. Rao, P. C. Eklund, R. E. Smalley, G. Dresselhaus, and M. S. Dresselhaus, Phys. Rev. B **58**, R16016 (1998).
[32] R. M. Martin and L. M. Falicov, Top. Appl. Phys. **8**, 79 (1975).
[33] B. C. Satishkumar, S. V. Goupalov, E. H. Haroz, and S. K. Doorn, Phys. Rev. B **74**, 155409 (2006).
[34] S. V. Goupalov, B. C. Satishkumar, and S. K. Doorn, Phys. Rev. B **73**, 115401 (2006).
[35] M. Machon, S. Reich, H. Telg, J. Maultzsch, P. Ordejon, and C. Thomsen, Phys. Rev. B **71**, 035416 (2005).
[36] S. V. Goupalov, Phys. Rev. B **71**, 153404 (2005); **72**, 159901(E)2005).
[37] R. Saito, G. Dresselhaus, and M. S. Dresselhaus, *Physical Properties of Carbon Nanotubes* (Imperial College Press, London, 1998).
[38] G. Bussi, J. Menendez, J. Ren, M. Canonico, and E. Molinari, Phys. Rev. B **71**, 041404(R) (2005).
[39] J. Jiang, R. Saito, A. Gruneis, S. G. Chou, Ge. G. Samsonidze, A. Jorio, G. Dresselhaus, and M. S. Dresselhaus, Phys. Rev. B **71**, 205420 (2005).
[40] K. Sato, R. Saito, J. Jiang, G. Dresselhaus, and M. S. Dresselhaus, Vib. Spectrosc. **45**, 89 (2007).